

## Electronic Supplementary Information (ESI)

### Exploring the 3D Structure and Defects of a Self-Assembled Gold Mesocrystal by Coherent X-ray Diffraction Imaging

Jerome Carnis, <sup>†a</sup> Felizitas Kirner, <sup>†b</sup> Dmitry Lapkin, <sup>‡a</sup> Sebastian Sturm, <sup>‡c</sup> Young Yong Kim, <sup>a</sup> Igor A. Baburin, <sup>d</sup> Ruslan Khubbutdinov, <sup>a,e</sup> Alexandr Ignatenko, <sup>a</sup> Ekaterina Iashina, <sup>f</sup> Alexander Mistonov, <sup>f</sup> Tristan Steegemans, <sup>b</sup> Thomas Wieck, <sup>c</sup> Thomas Gemming, <sup>c</sup> Axel Lubk, <sup>c</sup> Sergey Lazarev, <sup>a,g</sup> Michael Sprung <sup>a</sup> and Ivan A. Vartanyants, <sup>\*a,e</sup> Elena V. Sturm <sup>\*b</sup>

a. Deutsches Elektronen-Synchrotron DESY, Notkestrasse 85, D-22607 Hamburg, Germany, E-mail: ivan.vartanyants@desy.de.

b. University of Konstanz, Universitätsstraße 10, 78457 Konstanz, Germany, E-mail: elena.sturm@uni-konstanz.de.

c. Leibniz Institute for Solid State and Materials Research, Helmholtzstraße 20, 01069 Dresden, Germany

d. TU Dresden, Bergstraße 66b, 01062 Dresden, Germany

e. National Research Nuclear University MEPhI (Moscow Engineering Physics Institute), Kashirskoe shosse 31, 115409 Moscow, Russia

f. Saint-Petersburg State University, University Embankment 7/9, 199034 St Petersburg, Russia

g. Bruker AXS Advanced X-ray Solutions GmbH, Östliche Rheinbrückenstraße 49, 76187 Karlsruhe, Germany.

## Section S1. Sample preparation.

### Chemicals and Materials

Milli-Q water (resistivity 18.2 M $\Omega$ ·cm) was used in all experiments. All chemicals were bought and used as received. Hydrogen tetrachloroaurate trihydrate (HAuCl<sub>4</sub>·3H<sub>2</sub>O,  $\geq 99.9\%$ ), hexadecyltrimethylammonium bromide (CTAB,  $\geq 99\%$ ), cetyltrimethylammonium chloride solution (CTAC, 25 wt. % in H<sub>2</sub>O) and Hexadecylpyridinium chloride monohydrate (CPC, 99.0-102.0%) were purchased from Sigma-Aldrich. Sodium borohydride (NaBH<sub>4</sub>,  $\geq 97\%$ ) and L(+)-ascorbic acid (AA,  $\geq 99\%$ ) were purchased from Roth. Potassium bromide (KBr, for IR spectroscopy) was purchased from Merck. 1 mL shell vials were purchased from VWR. Silicon wafer in <100> orientation and dimensions of 5 × 7 mm<sup>2</sup> was purchased from Siegert Wafer and cleaned with dichloromethane and acetone before usage.

### Synthesis of Gold Seeds

An aqueous solution of HAuCl<sub>4</sub> (0.25 mL, 0.01 M) and an aqueous solution of CTAB (7.50 mL, 0.10 M) were mixed in a glass vial (50 mL) and tempered to 27 °C. 0.6 mL of 0.01 M freshly prepared, ice-cold NaBH<sub>4</sub> solution was added under vigorous stirring. The resulting solution turned brown immediately upon introduction of NaBH<sub>4</sub>. The seed solution was aged for 90 min at 27°C to ensure complete decomposition of excess borohydride.

### Synthesis of Gold Spheres

The synthesis of Gold Spheres was adapted from Zheng et al.<sup>1</sup> An aqueous solution of HAuCl<sub>4</sub> (1.00 mL, 0.01 M) and an aqueous solution of CTAC (39.00 mL, 0.10 M) were mixed in a glass vial (100 mL) and tempered to 27°C. An aqueous solution of AA (15.00 mL, 0.10 M) was added, followed by a rapid injection of 100  $\mu$ L of as prepared seeds. The solution turned red immediately and was kept at 27°C for 15 min. The spheres (1 mL) were collected by centrifugation at 9 000 rpm for 90 min, washed once with water and twice with aqueous 0.02 M CPC solution. The spheres were characterized by TEM and UV/Vis (Figure S1).

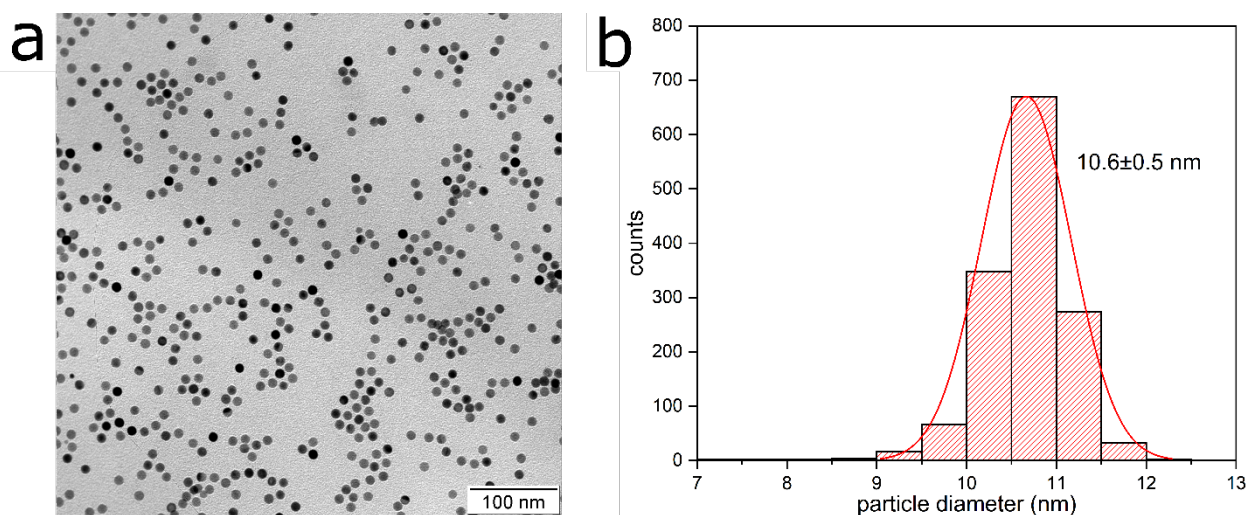


Figure S1. (a) TEM images of Gold Spheres, (b) particle-size distribution for (a) and (c) UV/Vis spectrum.

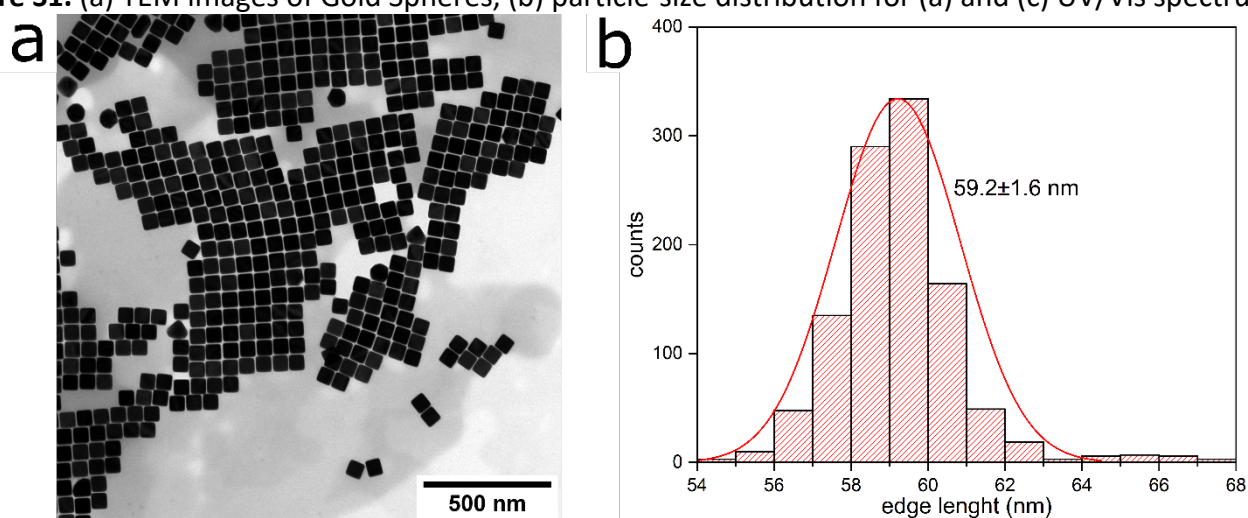


Figure S2. (a) TEM images of Gold Nanocubes and (b) particle-size distribution for (a).

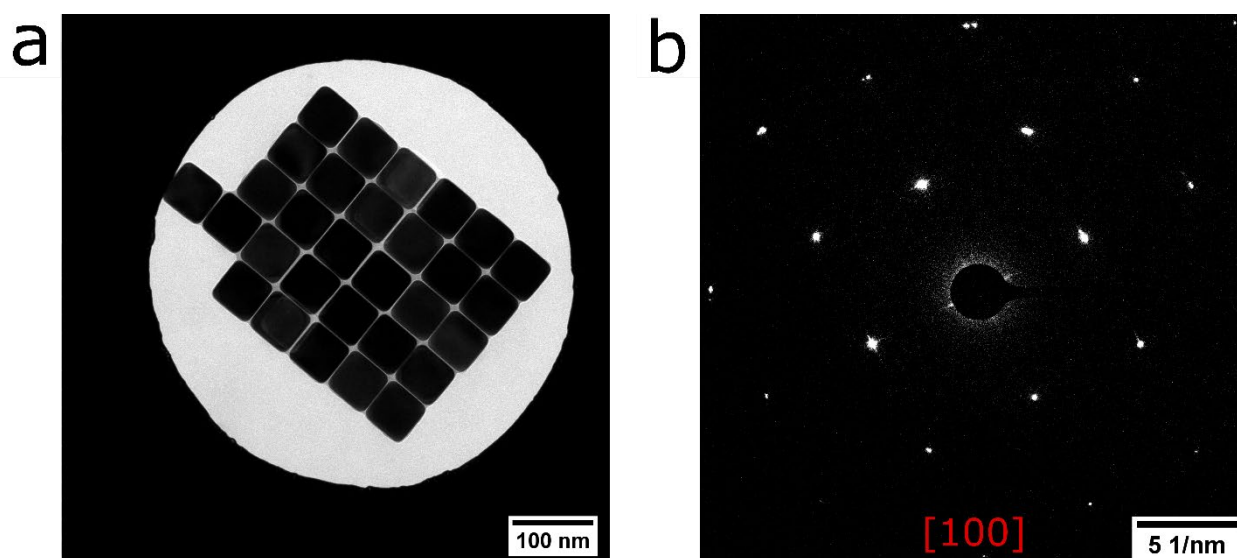
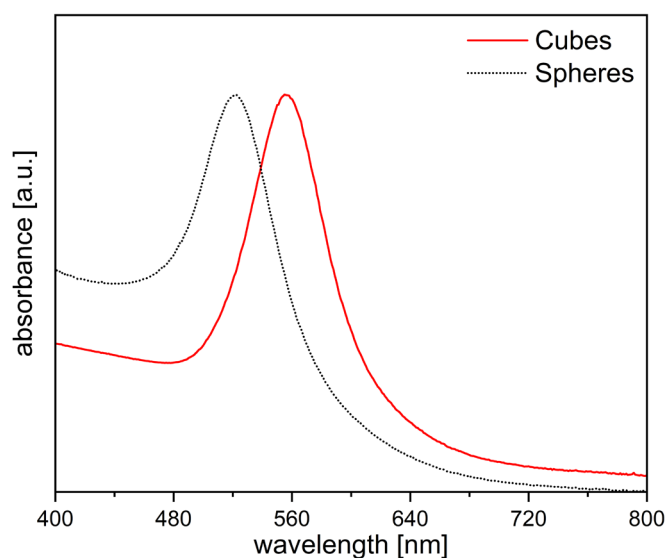
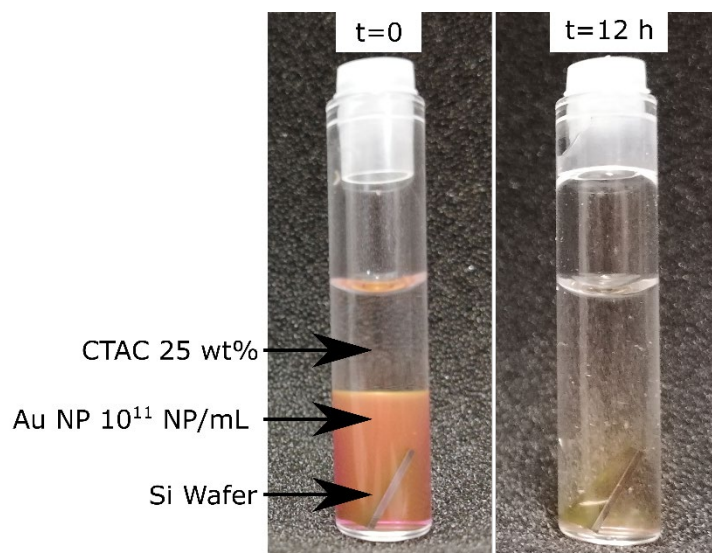


Figure S3. (a) TEM image of Gold Nanocubes and (b) the corresponding electron diffraction.



**Figure S4.** UV/Vis spectrum of Gold Spheres (dotted black) and Gold Nanocubes (solid red).



**Figure S5.** Exemplary setup for the preparation of self-assembled gold mesocrystals. First, the concentrated gold nanocube solution and a concentrated CTAC solution are carefully layered in a vial containing a silicon wafer. After 12 h, all particles are precipitated and assembled.

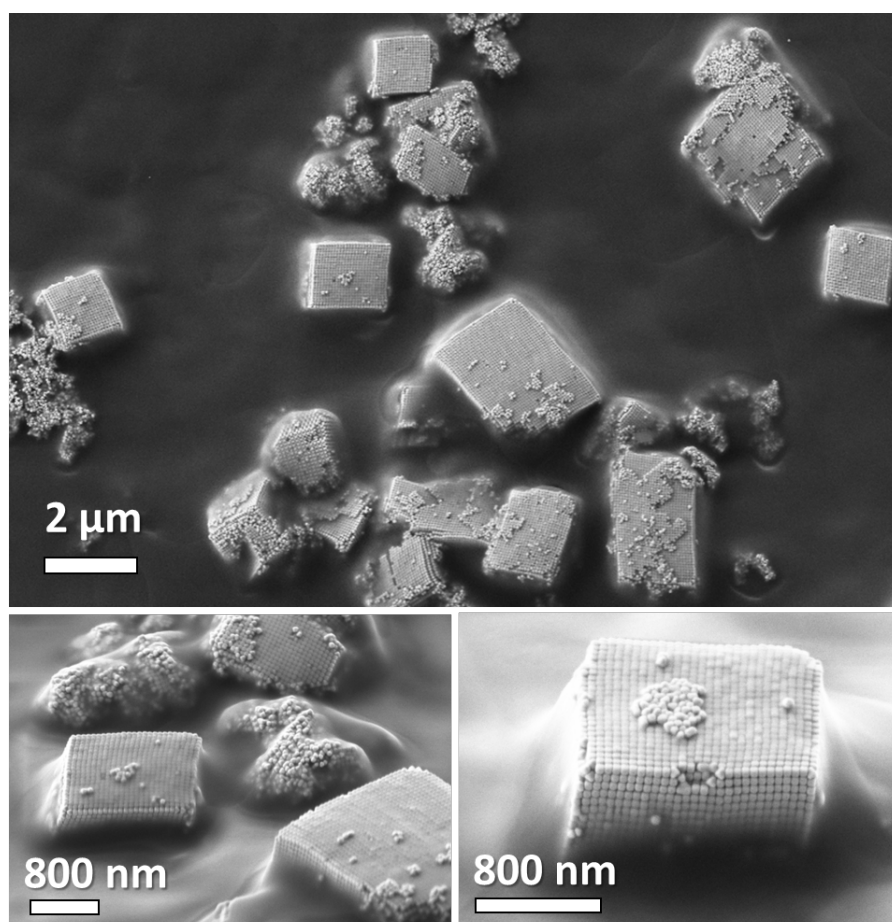


**Figure S6.** Exemplary SEM images of self-assembled gold mesocrystals. The slight displacement of lattice planes (visible on basal facets of mesocrystals) could be associated with the inhomogeneous crystal contraction during the drying processes and solvent evaporation. Also, local environmental perturbation could influence the assembly of nanocrystals.<sup>2-4</sup>

## Section S2. Phase retrieval

### Data preprocessing

In order to analyze the stack of diffraction images measured in the detector plane, the data needs to undergo several steps of preprocessing. For this purpose, we used the open-source BCDI python package.<sup>5</sup> First, the small-angle part corresponding to the zone shadowed by the beam stop (a Tungsten cylinder glued on a 100 μm-thick, 3 × 3 mm<sup>2</sup> Silicon wafer itself glued on a 100 μm-thick, 5 × 5 mm<sup>2</sup> Silicon wafer) was treated in the following way. For each 2D diffraction pattern the area corresponding to the Tungsten cylinder was masked, and the intensity in the area corresponding to the Silicon wafers was corrected to take into account X-ray absorption at 8.7 keV. Then, the data lying in the cylindrical detector frame (rocking angle, detector vertical axis, and detector horizontal axis) was interpolated into the orthonormal

laboratory frame using linear interpolation and neglecting the curvature of Ewald sphere. This may be done as soon as the momentum transfer at the edge of the region of interest used for phase retrieval was  $\sim 0.57899 \text{ nm}^{-1}$  considering the curvature of Ewald sphere and it was  $\sim 0.57854 \text{ nm}^{-1}$  when the curvature was neglected. Therefore, the difference in momentum transfer was about  $0.00045 \text{ nm}^{-1}$  which corresponds to a direct space length of  $\sim 14 \mu\text{m}$ . This length is much larger than the mesocrystal size ( $\sim 1.25 \mu\text{m} \times 1.25 \mu\text{m} \times 1.5 \mu\text{m}$ ) and gives the confidence that the curvature of the Ewald sphere can be neglected in the conditions of our experiment.

### Resolution estimate

The resolution of the reconstruction was estimated using the normalized Phase-Retrieval Transfer Function<sup>6</sup> (PRTF) at a cutoff value of  $1/e$  (see Figure S7d). The PRTF is a measure of how well the retrieved Fourier amplitudes match the square root of the measured diffraction intensity. After calculating the ratio of the reconstructed and measured amplitudes, the obtained 3D PRTF was azimuthally averaged over shells of constant  $q$  and normalized to obtain the result shown in Figure S7d. Measured voxels of zero intensity were excluded from the PRTF calculation.

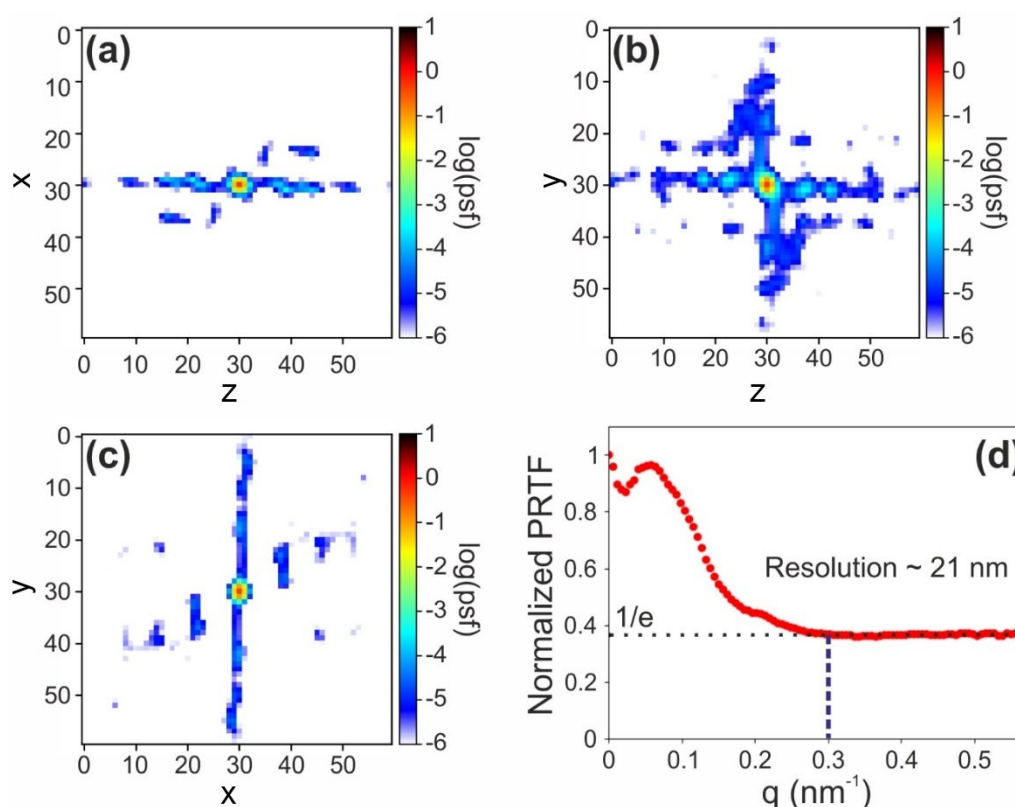


**Fig. S7.** (a-c) Slices through the point spread function obtained from application of the Lucy-Richardson algorithm, (d) Azimuthally averaged and normalized PRTF. The resolution is determined as the cross-over between the PRTF and the  $1/e$  line.

### Section S3. Angular X-ray Cross-Correlation Analysis

The Angular X-ray Cross-Correlation Analysis (AXCCA) is a recently emerging technique to study angular correlation in the scattered intensities in an X-ray experiment. The detailed description of the method can be found for example in Ref.<sup>7</sup>. Typically, this method is applied to the collected 2D diffraction patterns, however, in this experiment we collected intensity distribution in 3D reciprocal space. Here, we adapt AXCCA to take into account the additional degree of freedom.<sup>8</sup>

The modified technique is based on calculation of the cross-correlation function (CCF)

$$C(q_1, q_2, \Delta) = \langle I(\mathbf{q}_1)I(\mathbf{q}_2)\delta\left(\frac{\mathbf{q}_1 \cdot \mathbf{q}_2}{\|\mathbf{q}_1\|\|\mathbf{q}_2\|} - \cos \Delta\right) \rangle, \quad (\text{S1})$$

where  $I(\mathbf{q}_1)$  and  $I(\mathbf{q}_2)$  are the scattered intensities taken at the momentum transfer vectors  $\mathbf{q}_1$  and  $\mathbf{q}_2$  with the relative angle  $\Delta$  between them. The averaging in Eq. S1 is performed over all vector positions  $\mathbf{q}_1$  and  $\mathbf{q}_2$  with the modulus of the momentum transfer values  $q_1$  and  $q_2$ , respectively. In the case of the crystalline sample, the resulting CCFs contain peaks at the relative angles between the Bragg peaks, *i.e.* the angles between a certain pair of the families of crystallographic planes. These angles provide additional information about the crystalline structure in comparison to the conventional analysis of the radial intensity distribution.

#### Unit cell parameters determination

There are four most prominent peaks in the intensity radial profile at momentum transfer values  $q_1 = 0.104 \text{ nm}^{-1}$ ,  $q_2 = 0.144 \text{ nm}^{-1}$ ,  $q_3 = 0.172 \text{ nm}^{-1}$  and  $q_4 = 0.208 \text{ nm}^{-1}$  as shown in Figure 3c of the main text. We calculated the CCFs for all possible combinations of these  $q$  values. We found that the peak positions do not fit a simple cubic lattice that was an initial guess for the superlattice structure. Instead, we assumed the crystallographic lattice to be a primitive one (space group  $P1$ ). The expected peak positions for a primitive cell were calculated as the angles between the certain sets of equivalent crystallographic directions. Tuning the unit cell parameters of this primitive cell, we matched the position of the peaks from the experimentally determined CCFs with the ones obtained for the primitive structure. One should note, that at each  $q$  value we observe contribution of different reflections due to the large width of Bragg peaks, for example, at  $q_1$  there are correlations between 100, 010, and 001 Bragg peaks. The resulting CCFs with the calculated peak positions for optimized primitive and simple cubic structures are shown in Figure S8 and Figure S9.

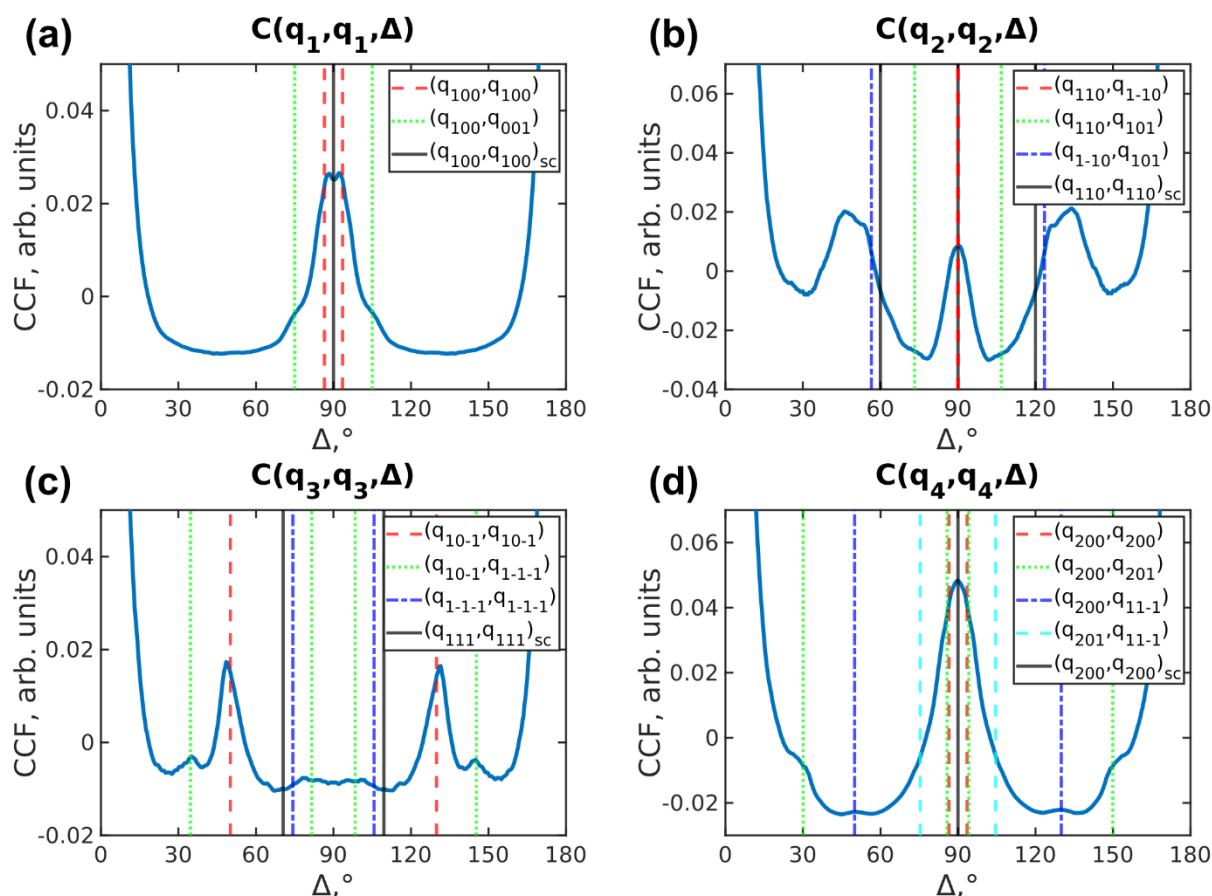


**Figure S8.** CCFs calculated for the intensities taken at the same momentum transfer values: (a)  $q_1 = 0.104 \text{ nm}^{-1}$ , (b)  $q_2 = 0.144 \text{ nm}^{-1}$ , (c)  $q_3 = 0.172 \text{ nm}^{-1}$ , and (d)  $q_4 = 0.208 \text{ nm}^{-1}$ . The corresponding peak positions for the optimized primitive unit cell are shown with the vertical colored dashed lines. The peak positions for a simple cubic unit cell are shown with the vertical black lines.

The obtained parameters of the primitive unit cell are the following:  $a = b \approx 63.2 \pm 0.1 \text{ nm}$ ,  $c \approx 62.2 \pm 0.1 \text{ nm}$ ,  $\alpha = \beta \approx 75 \pm 1^\circ$ ,  $\gamma \approx 90 \pm 1^\circ$ . As one can see in Figure S8 and Figure S9, the peak positions in the experimental CCFs are in a good agreement with this model. The only exception are the CCFs calculated for the intensities taken at  $q_2 = 0.144 \text{ nm}^{-1}$ , where the peaks deviate from the expected positions. This divergence can be explained by the contribution of correlations between the Bragg peaks and anisotropic features of the form-factor of the nanocubes, which are discussed below.

The calculated Bragg peak positions for the optimized primitive structure are shown in Figure S10. Some of the Bragg peaks do not contribute to the intensity radial profile because they are suppressed by the NC's form-factor minima. Others have different intensities due to various defects in the superlattice affecting the structure factor values. However, even when the Bragg peaks are not prominent in the radial profile, they may contribute to the CCFs.

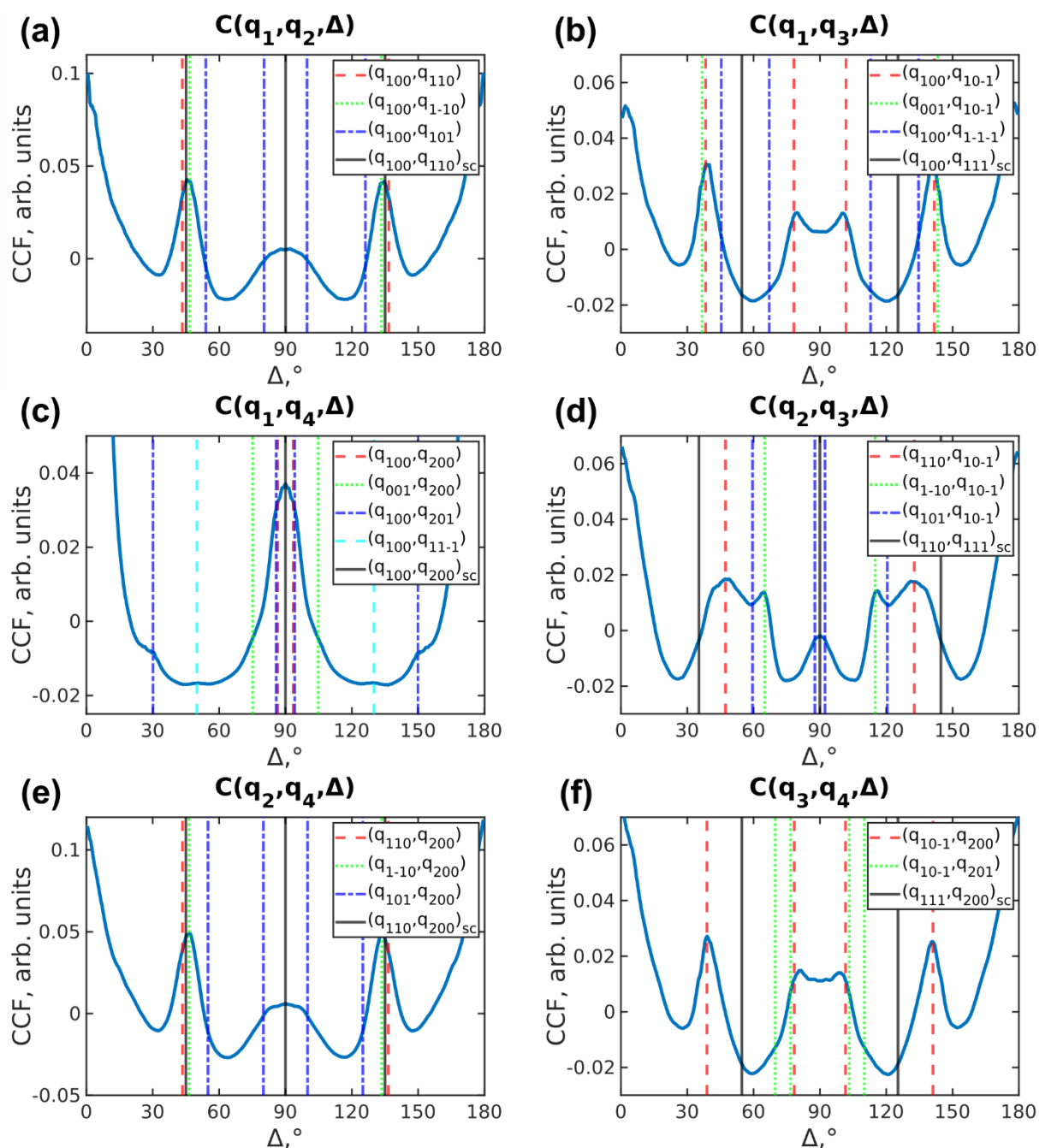


**Figure S9.** CCFs calculated for the intensities taken at two different momentum transfer values: (a)  $q_1 = 0.104 \text{ nm}^{-1}$  and  $q_2 = 0.144 \text{ nm}^{-1}$ , (b)  $q_1 = 0.104 \text{ nm}^{-1}$  and  $q_3 = 0.172 \text{ nm}^{-1}$ , (c)  $q_1 = 0.104 \text{ nm}^{-1}$  and  $q_4 = 0.208 \text{ nm}^{-1}$ , (d)  $q_2 = 0.144 \text{ nm}^{-1}$  and  $q_3 = 0.172 \text{ nm}^{-1}$ , (e)  $q_2 = 0.144 \text{ nm}^{-1}$  and  $q_4 = 0.208 \text{ nm}^{-1}$  and (f)  $q_3 = 0.172 \text{ nm}^{-1}$   $q_4 = 0.208 \text{ nm}^{-1}$ . The corresponding peak positions for the optimized primitive unit cell are shown with the vertical colored dashed lines. The peak positions for a simple cubic unit cell are shown with the vertical black lines.

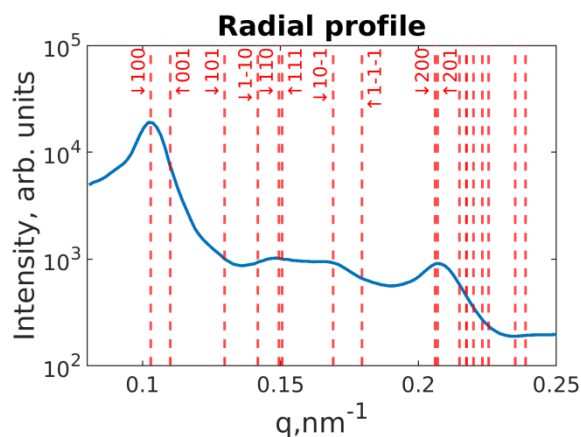


**Figure S10.** Angular averaged radial profile of the scattered intensity with the subtracted background (blue line). The red vertical dashed lines show the positions of the Bragg peaks for the optimized primitive unit cell model determined in this work.

### Section S4. Nanocubes orientation determination

The scattered intensity contains the form-factor of the NCs which modulates the structure factor of the superlattice, leading to the absence of certain Bragg peaks. At the same time, at some  $q$  values (for example, at  $q = 0.477 \text{ nm}^{-1}$ ) the maximum of the form-factor coincides with the minimum of the structure factor as shown in Figure S11a. At such  $q$  values, the angular distribution of the form-factor can be studied.

The anisotropy of the cubic form-factor gives additional information about the angular orientation of the nanocubes inside the superlattice. In order to find this orientation, we first determined the orientation of the direction vectors  $\mathbf{b}_1$ ,  $\mathbf{b}_2$  and  $\mathbf{b}_3$  collinear with the reciprocal basis vectors of the superlattice from the first order Bragg peaks positions at  $q = 0.104 \text{ nm}^{-1}$  as shown in Figure S11b. From these reciprocal vector directions, the direction of the vectors  $\mathbf{a}_1$ ,  $\mathbf{a}_2$ , and  $\mathbf{a}_3$  collinear with the real space basis vectors of the superlattice were calculated. Their directions are also shown in Figure S11b. Then, we studied the intensity distribution at  $q = 0.477 \text{ nm}^{-1}$  shown in Figure S11c. There are six prominent maxima at this  $q$  value along the directions normal to the facets of the NCs. From the figure, one can see that these maxima are misaligned with the direction vectors  $\mathbf{a}_1$ ,  $\mathbf{a}_2$ , and  $\mathbf{a}_3$  of the superlattice.

In order to find this misalignment, we found a maximum of the correlation  $\langle I_{exp}(\mathbf{q})I_{sim}(\mathbf{q}) \rangle_{|q|=q}$  between the experimental intensity  $I_{exp}(\mathbf{q})$  and the model one  $I_{sim}(\mathbf{q})$  at  $q = 0.477 \text{ nm}^{-1}$ . The simulated model intensity was the form-factor of nanocubes with the normally distributed sizes with  $\langle d \rangle = 59.0 \text{ nm}$  and  $\sigma_d = 1.2 \text{ nm}$ . Initially, the nanocubes (100) and (010) facets were aligned with the axes  $\mathbf{a}_1$  and  $\mathbf{a}_2$  as shown in Figure S11d. Then the cubes were consequently rotated around the fixed (motionless) axes  $\mathbf{a}_1$ ,  $\mathbf{a}_2$ , and  $\mathbf{a}'_3 = \mathbf{a}_1 \times \mathbf{a}_2$  by angles  $\varphi$ ,  $\vartheta$  and  $\psi$ , respectively (so-called extrinsic rotations in the formalism of

Tait–Bryan angles).<sup>9</sup> For each angular position, the form-factor intensity was calculated and correlated with the experimental one. The maximum of correlation was found to be at  $\varphi = -13 \pm 1^\circ$ ,  $\vartheta = 7 \pm 1^\circ$  and  $\psi = -4 \pm 1^\circ$ . The orientation of the nanocubes corresponding to these angles is shown in Figure S11e, the corresponding form-factor is shown in Figure S11f. The misalignment angles between  $\mathbf{a}_1$ ,  $\mathbf{a}_2$ , and  $\mathbf{a}_3$  directions of the superlattice and the closest normal to facets of the nanocubes are about  $8^\circ$ ,  $13^\circ$ , and  $6^\circ$ , respectively. Noteworthy, the features in the experimental intensity are broader than the ones in the model form factor, that implies angular disorder of the nanocubes around the obtained average orientation.

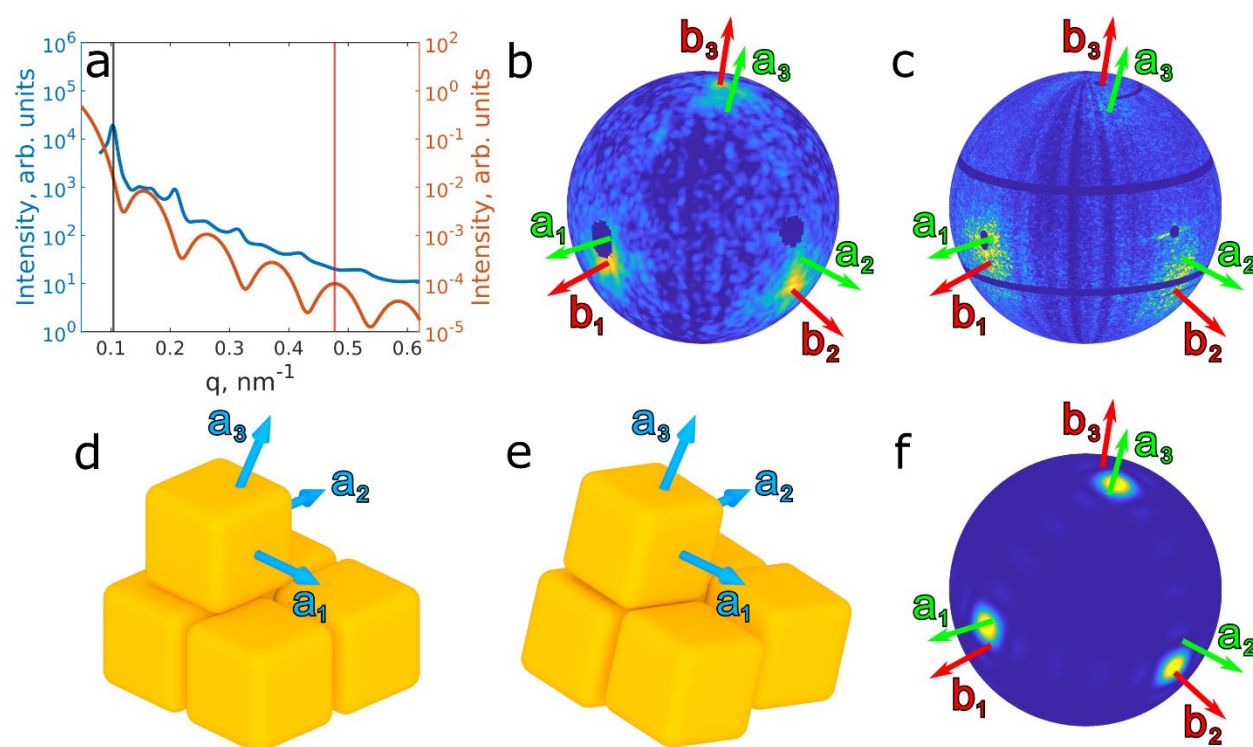


**Figure S11.** (a) Experimental averaged radial profile (blue) and calculated isotropic form-factor of the nanocubes (red) with parameters  $\langle d \rangle = 59.0$  nm and  $\sigma_d = 1.2$  nm. The black vertical line is at  $q = 0.104$  nm<sup>-1</sup>, where the first order Bragg peaks are located. The red vertical line is at  $q = 0.477$  nm<sup>-1</sup>, where the form-factor was studied. (b) Experimental intensity distribution at  $q = 0.104$  nm<sup>-1</sup> corresponding to the first order Bragg peaks. The red arrows show the reciprocal basis vectors aligned with the Bragg peaks. The green arrows show the directions of the real space basis vectors of the superlattice. (c) Experimental intensity distribution at  $q = 0.104$  nm<sup>-1</sup> corresponding to the 4<sup>th</sup> order maxima of the form-factor. The bright spots are attributed to the form-factor maxima normal to the facets of the nanocubes. (d) Initial real space model of the superlattice including the nanocubes aligned with  $\mathbf{a}_1$  and  $\mathbf{a}_2$  superlattice basis vectors. (e) Real space model where the nanocubes are oriented according to the maximum of the correlation between the experimental and simulated intensity distribution at  $q = 0.477$  nm<sup>-1</sup>. (f) Simulated 3D intensity distribution of the form-factor at  $q = 0.477$  nm<sup>-1</sup> for the nanocubes orientated as in (e).

## Section S5. Structural analysis of the mesocrystal grain based on the reconstructed electron density

For evaluation of the superlattice strain the data has been processed in python in the following way. First, the original dataset of  $137 \times 169 \times 170$  voxels was sampled up twice. Then, different parameters for Gaussian filtering (with sigma 0.5 px and 1 px) were applied, also in combination with different thresholds (ranging from 0.3 to 0.9 of maximum electron density). Finally, a 3D labeling algorithm (`scipy.ndimage.label`) using the Python library SciPy<sup>10, 11</sup> was used to find nanoparticle positions. In order to ensure that all found positions are reliable, only particles with a bounding box of size  $3 \times 3 \times 3$  to  $12 \times 12 \times 12$  and a volume of 125 to 512 voxels were considered as correct. These criteria were chosen to favoring quality of found positions over quantity, yielding a dataset of sufficiently many automatically found NP positions.

An ideal lattice has been modeled after the average unit cell was retrieved by the AXCCA. The displacement vector  $\mathbf{u}_i$  for each NP position  $\mathbf{r}_{real,i}$  to the nearest position in the ideal lattice  $\mathbf{r}_{ideal,i}$  has been calculated as

$$\mathbf{u}_i = \mathbf{r}_{real,i} - \mathbf{r}_{ideal,i} \quad (\text{S2})$$

(see Figure 6 from the main text).

Thus, obtained displacement vectors were interpolated on a Cartesian grid using nearest neighbor interpolation, representing the displacement field. To be sure that all displacements will be corresponding to one unit cell of the lattice and the particle positions will not belong to the next unit cell we introduced 27 translational offsets of the ideal lattice by  $1/3$  or  $2/3$  of the unit cell

$$\mathbf{r}_{ideal,i}^* = \mathbf{r}_{ideal,i} + \frac{k}{3} \mathbf{a}_1 + \frac{l}{3} \mathbf{a}_2 + \frac{m}{3} \mathbf{a}_3, \quad (\text{S3})$$

where  $k, l, m$  can be one of the integer numbers 0, 1 or 2 and compared real positions  $\mathbf{r}_{real,i}$  with the new ideal ones  $\mathbf{r}_{ideal,i}^*$ .

The median, obtained over all different translational offsets, has been calculated for the derivative of each displacement field vector component in each direction  $\partial u_i / \partial x_j$ . Afterwards, a Gaussian filter with the standard deviation  $\sim 70$  nm has been applied to reduce interpolation artifacts and noise.

The strain tensor components were derived as<sup>12</sup>

$$\varepsilon_{ij} = \frac{1}{2} \left( \frac{\partial u_i}{\partial x_j} + \frac{\partial u_j}{\partial x_i} \right), \quad (\text{S4})$$

(see Figure 7 in the main text and Figures S15-S20).

The rotation matrix was evaluated as

$$\omega_{ij} = \frac{1}{2} \left( \frac{\partial u_i}{\partial x_j} - \frac{\partial u_j}{\partial x_i} \right), \quad (\text{S5})$$

(see Figure 7 in the main text and Figures S21-S23).

From the strain tensor we obtained the dilation as

$$e = \varepsilon_{11} + \varepsilon_{22} + \varepsilon_{33}, \quad (\text{S6})$$

(see Figure 7 in the main text and Figure S14).

This definition of a strain tensor is of course only valid for small lattice deformations. Therefore, in order to verify the fidelity of the retrieved strain tensor field (and rotation matrix), it has been reapplied to an ideal lattice (see Figure S24).

For this, first an ideal lattice using the average unit cell retrieved by the AXCCA was created. This lattice was then deformed by applying the calculated strain tensor and rotation matrix. Finally, the outer shape of the original crystal (as determined by a threshold) has been cut from this deformed lattice, which of course leads to slightly rougher surfaces in the model than the original crystal facets. Nevertheless, the yielded model bears a very close resemblance to the original data, thus confirming the justification of afore made assumptions. As can be seen in the corresponding slices (b,c,d) through the crystal, in most regions, the lattice deformations of the model (red) follow the same trend as in the underlying original crystal (yellow).

From this model the actual number of NPs in the whole crystal can also be approximated quite reliably to be around 8200 in total.

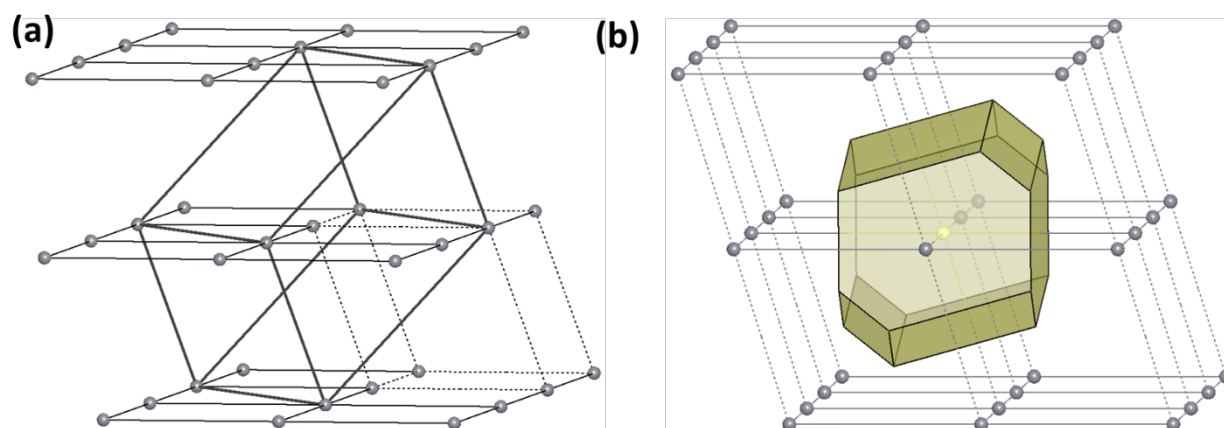


**Figure S12.** (a) Relationship between primitive (black dotted line) and conversional monoclinic I-centred (black solid line) cells. (b) Square layers with a monoclinic offset give rise to a distorted primitive cubic packing.

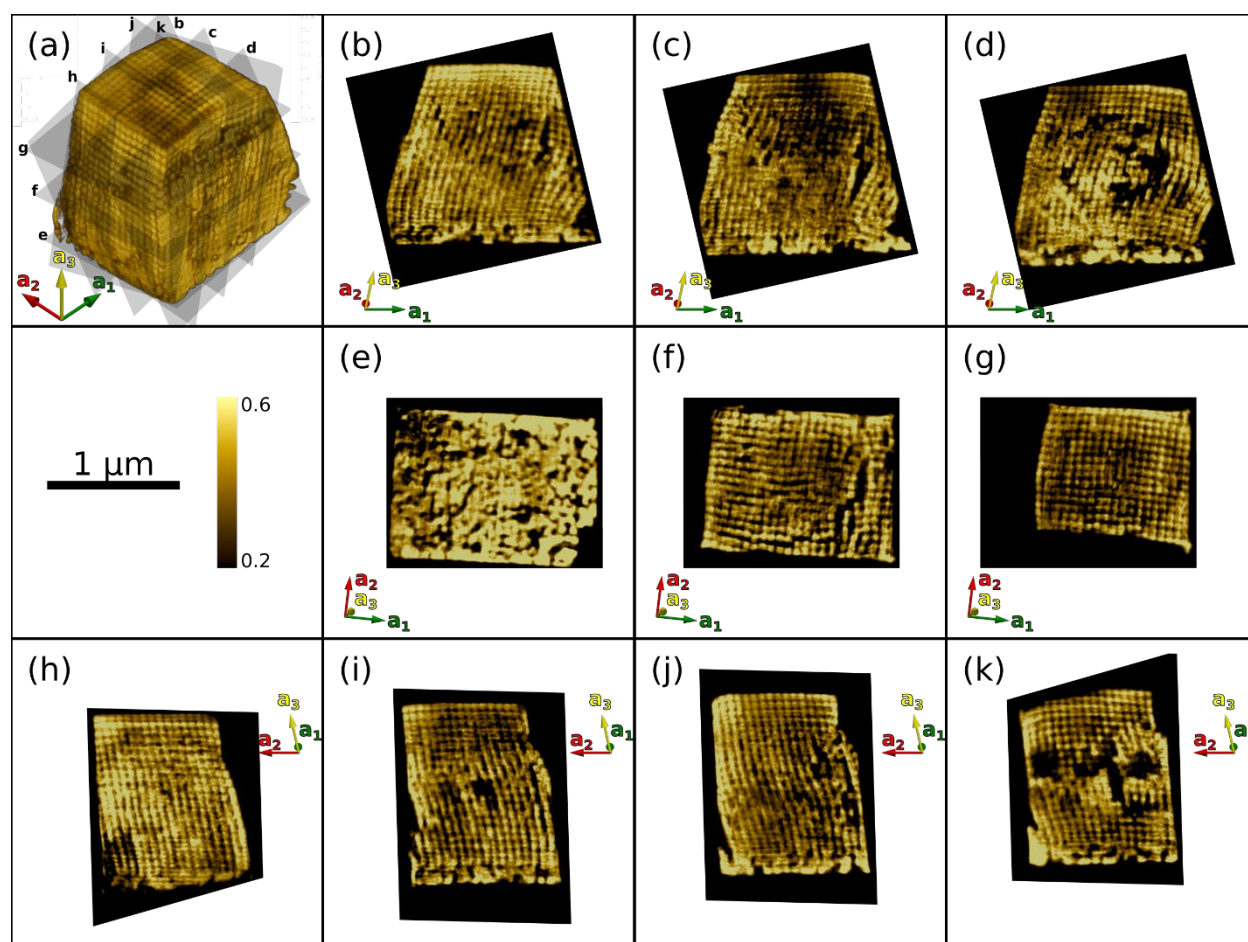


**Figure S13.** a) Volume rendering of reconstructed 3D electron density with position of following 2D slices indicated.  $\{010\}$  (b-d),  $\{001\}$  (e-g) and  $\{100\}$  (h-k) 2D slices of the reconstructed mesocrystal. The positions of slices are indicated in (a)

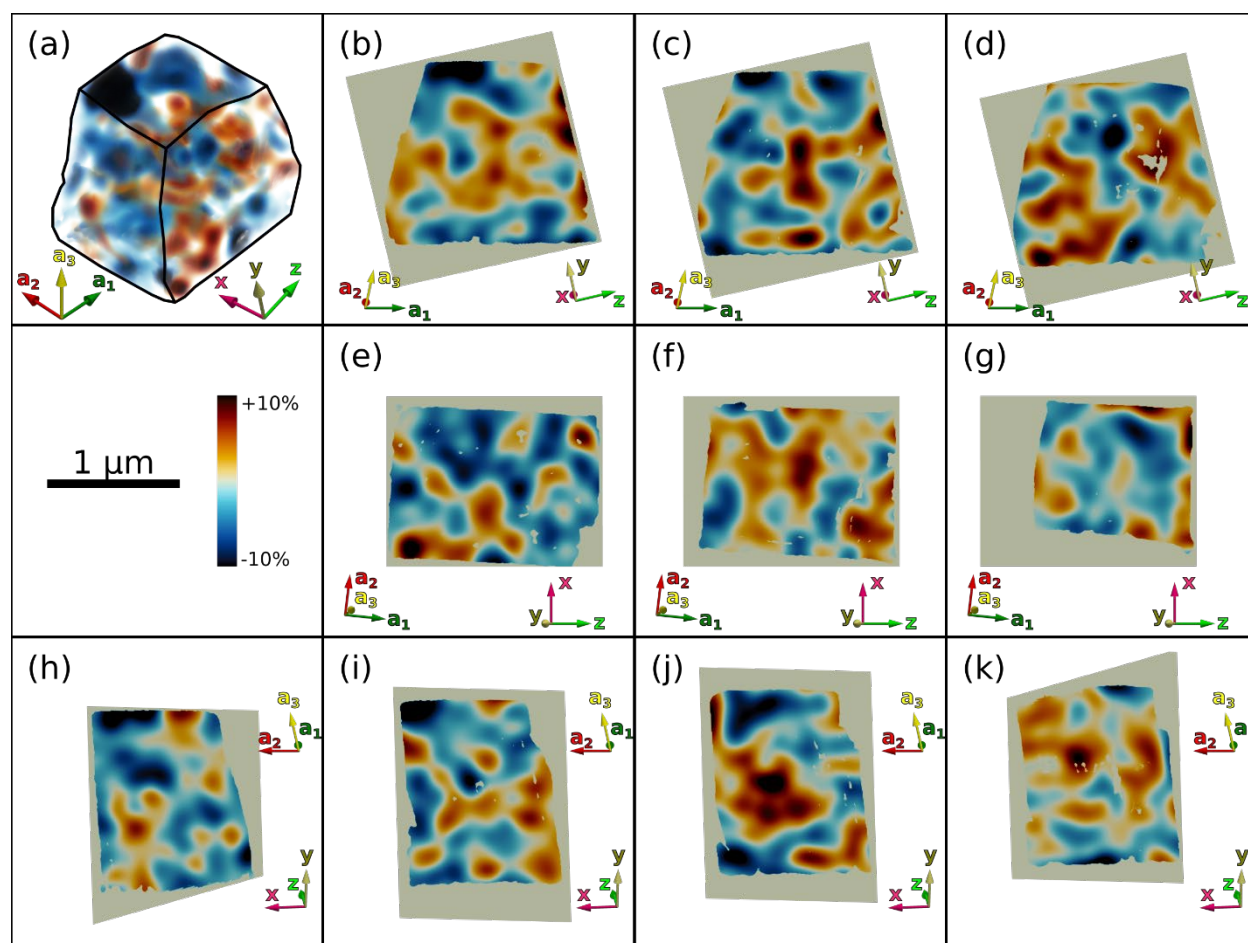


**Figure S14.** a) Volume rendering of the 3D superlattice dilatation map. {010} (b-d), {001} (e-g) and {100} (h-k) 2D slices of dilatation map, sliced the same way as in Figure S12.

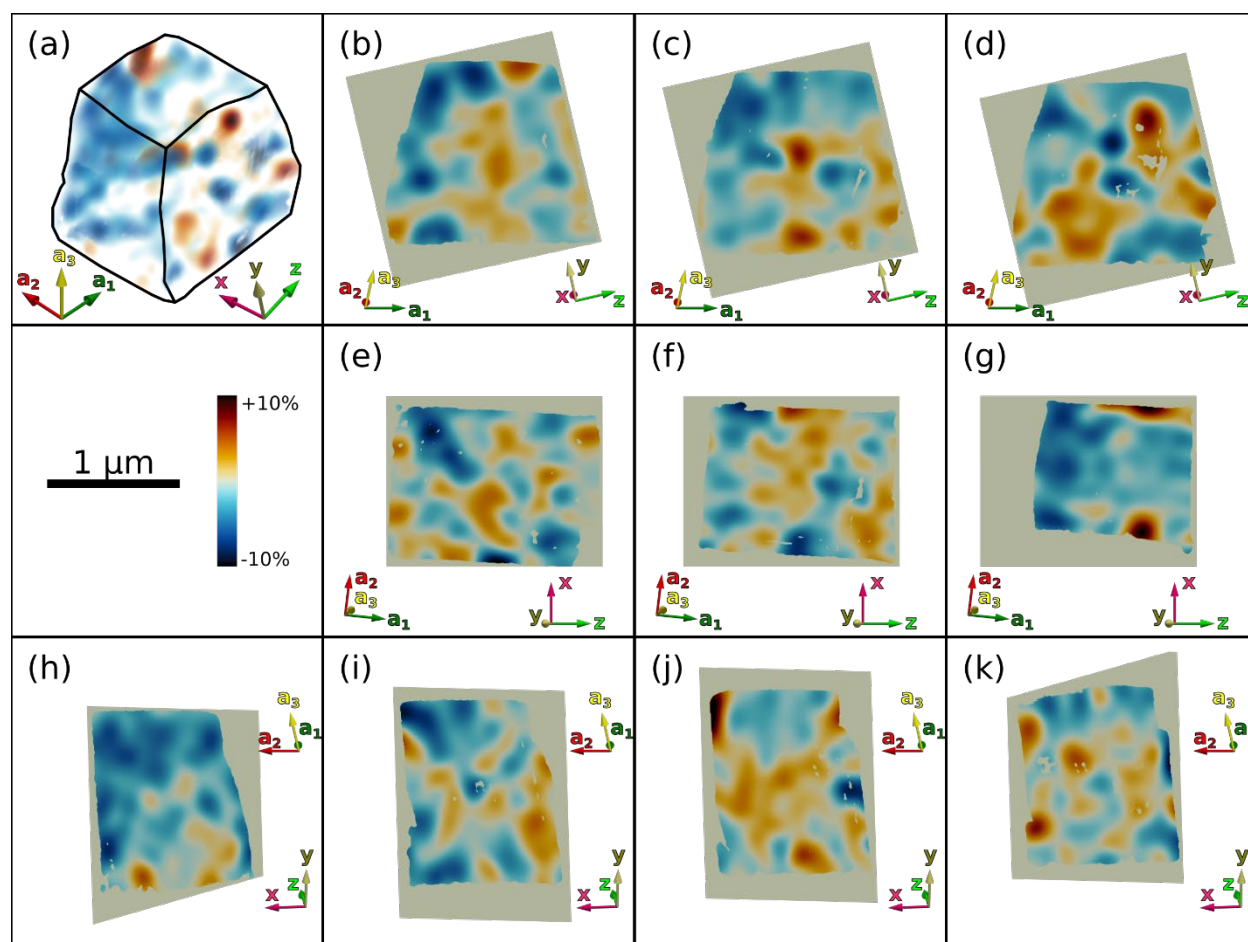


**Figure S15.** a) Volume rendering of the  $\epsilon_{xx}$  superlattice strain tensor component. {010} (b-d), {001} (e-g) and {100} (h-k) 2D slices through this strain tensor component, sliced the same way as in Figure S12.

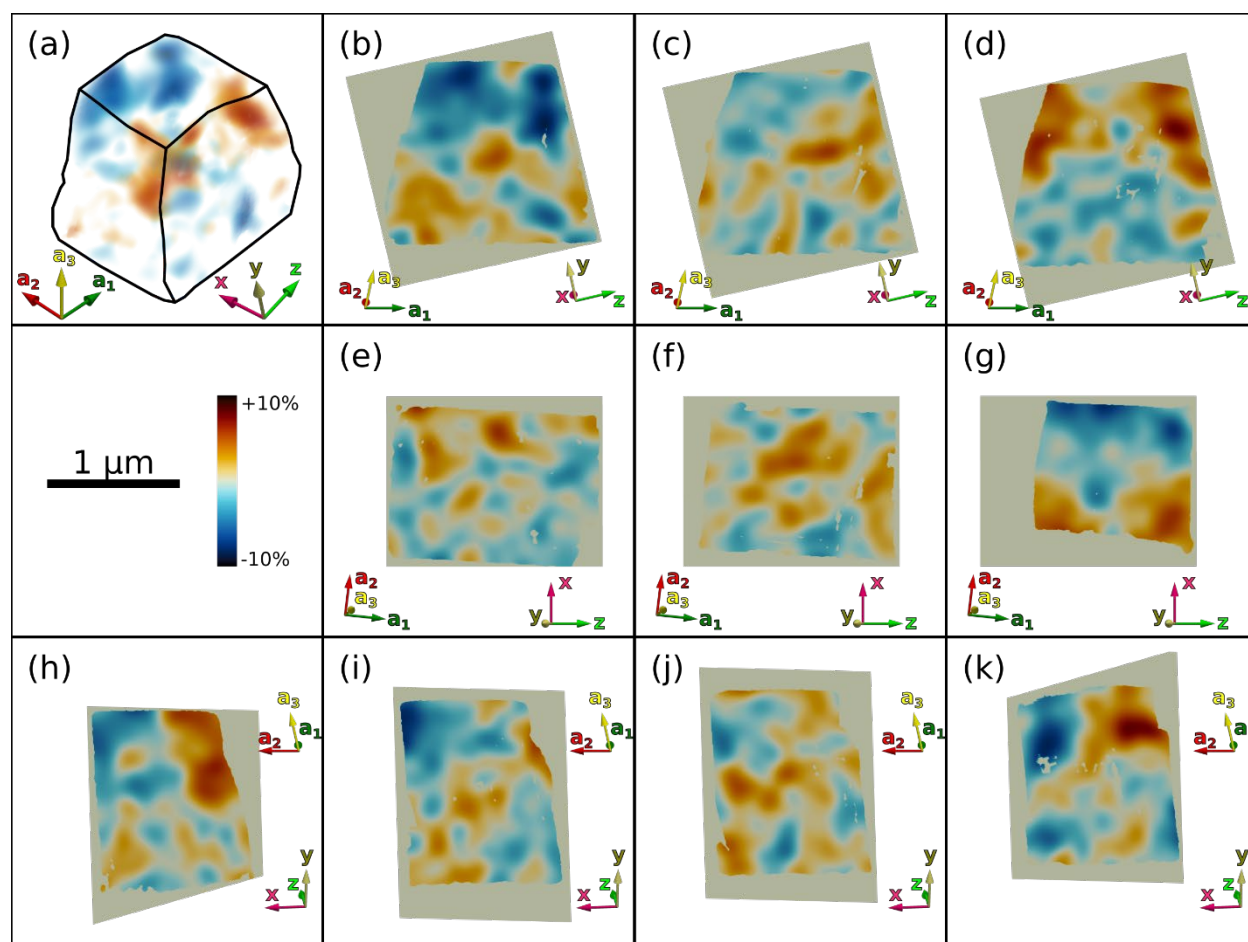


**Figure S16.** a) Volume rendering of the  $\epsilon_{xy}$  superlattice strain tensor component. {010} (b-d), {001} (e-g) and {100} (h-k) 2D slices through this strain tensor component, sliced the same way as in Figure S12.

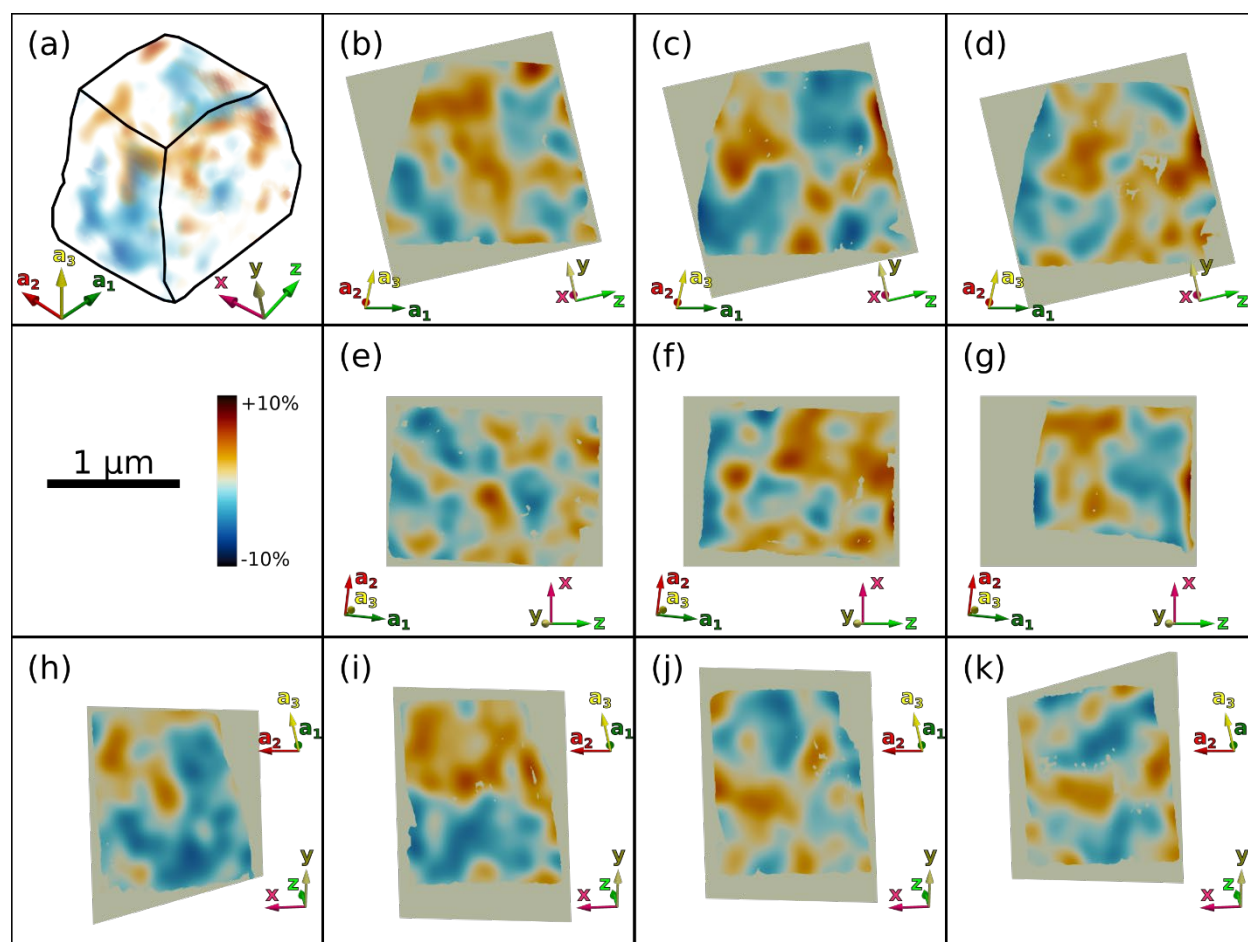


**Figure S17.** a) Volume rendering of the  $\epsilon_{xz}$  superlattice strain tensor component.  $\{010\}$  (b-d),  $\{001\}$  (e-g) and  $\{100\}$  (h-k) 2D slices through this strain tensor component, sliced the same way as in Figure S12.

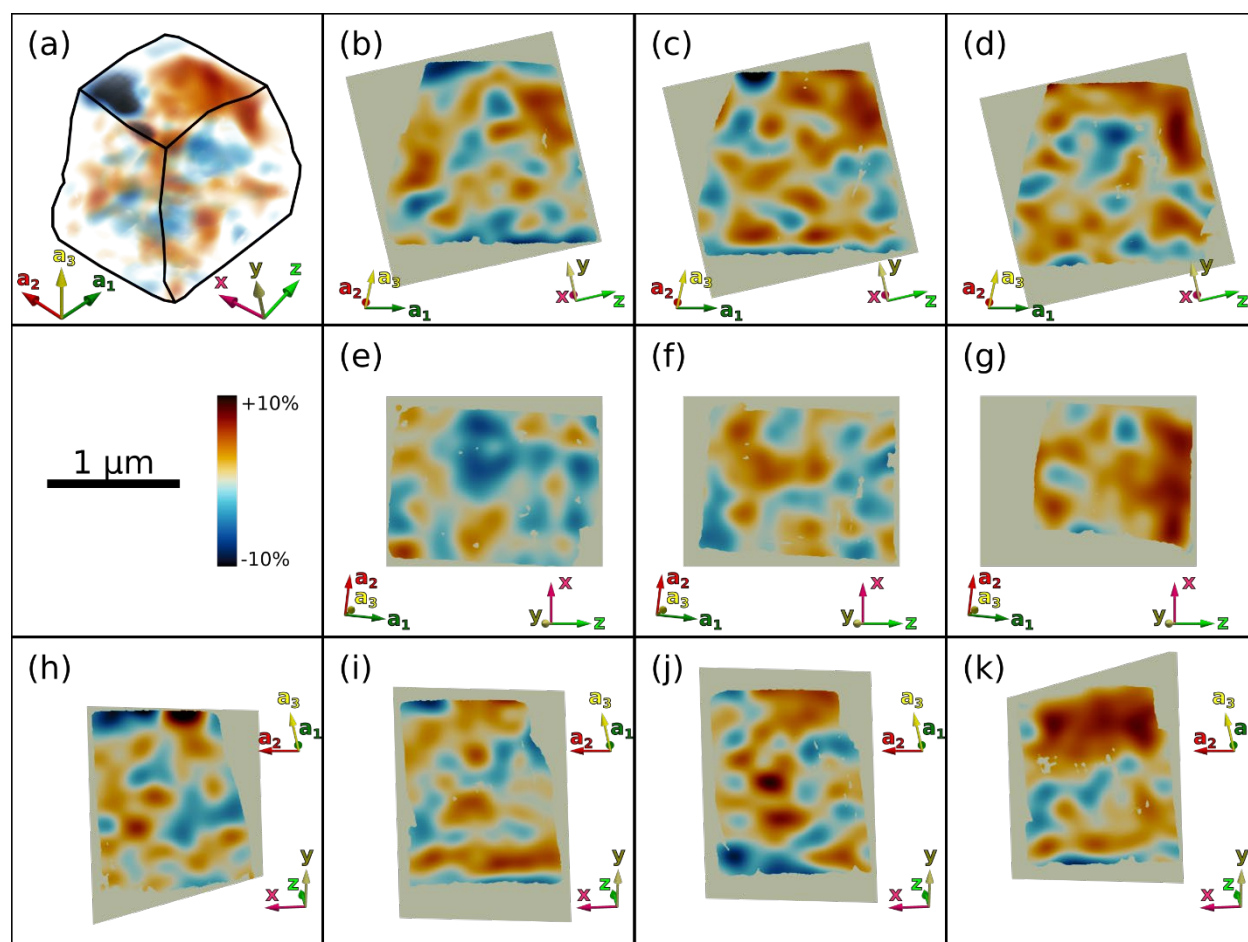


**Figure S18.** a) Volume rendering of the  $\epsilon_{vv}$  superlattice strain tensor component. {010} (b-d), {001} (e-g) and {100} (h-k) 2D slices through this strain tensor component, sliced the same way as in Figure S12.

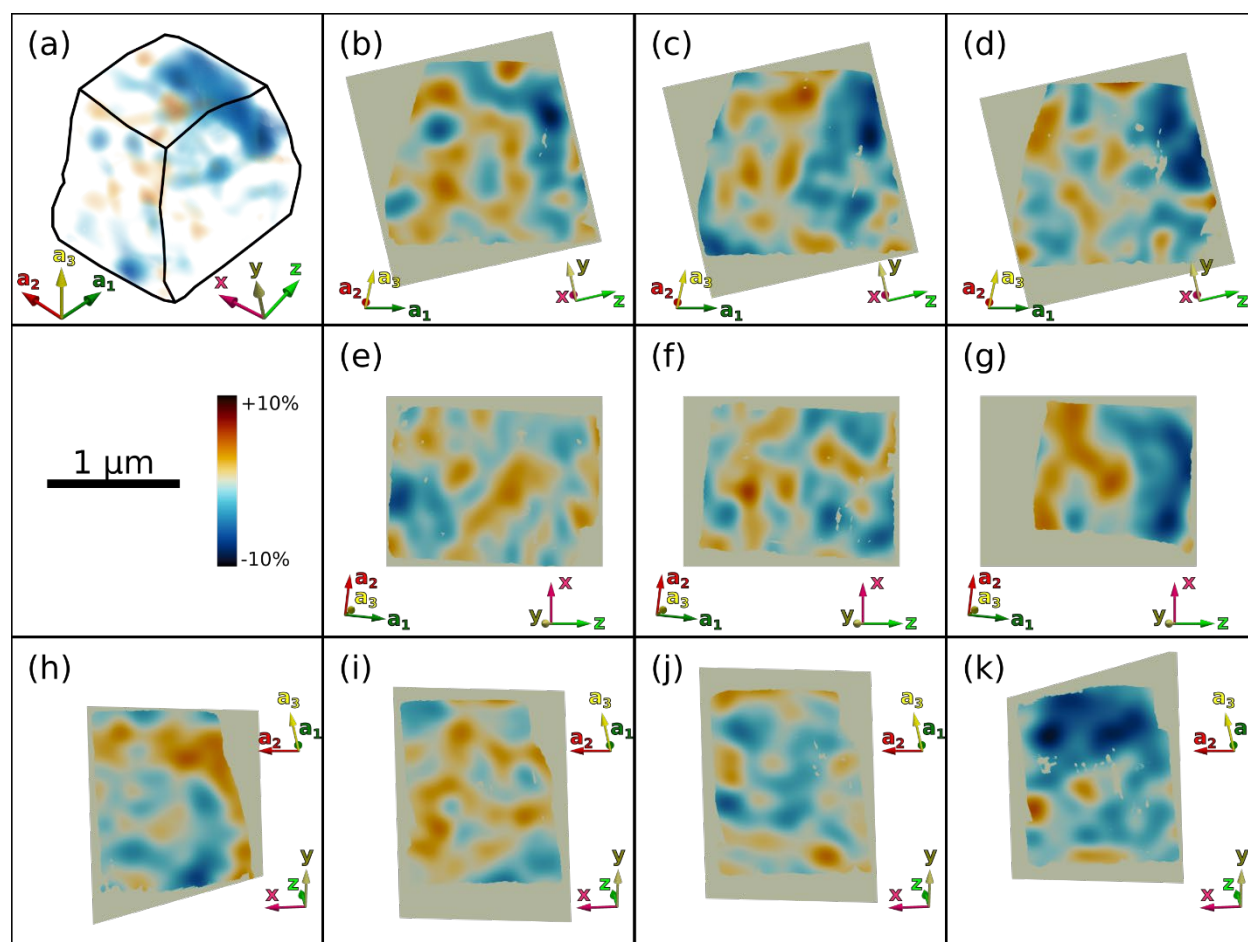


**Figure S19.** a) Volume rendering of the  $\epsilon_{vz}$  superlattice strain tensor component. {010} (b-d), {001} (e-g) and {100} (h-k) 2D slices through this strain tensor component, sliced the same way as in Figure S12.

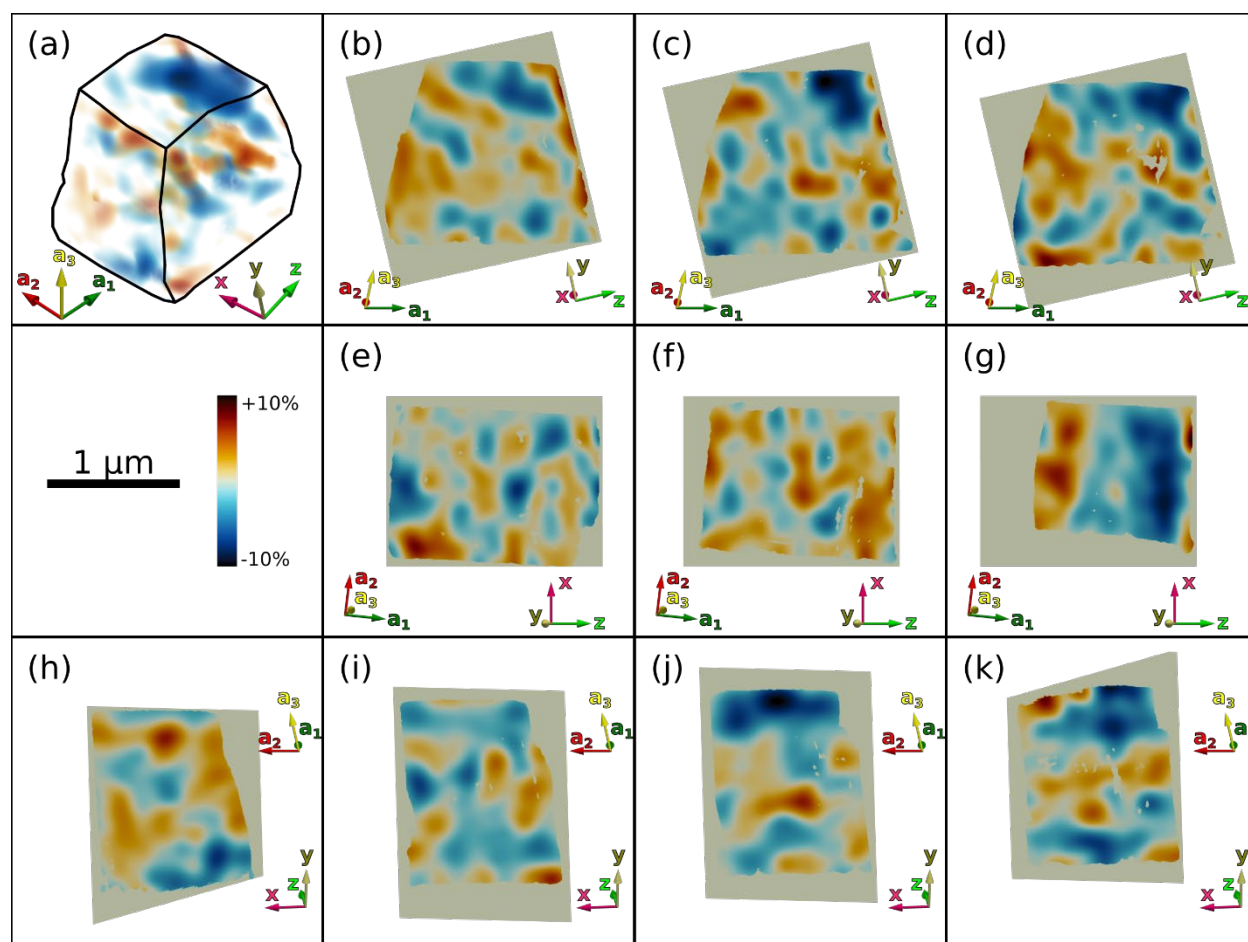


**Figure S20.** a) Volume rendering of the  $\epsilon_{zz}$  superlattice strain tensor component. {010} (b-d), {001} (e-g) and {100} (h-k) 2D slices through this strain tensor component, sliced the same way as in Figure S12.

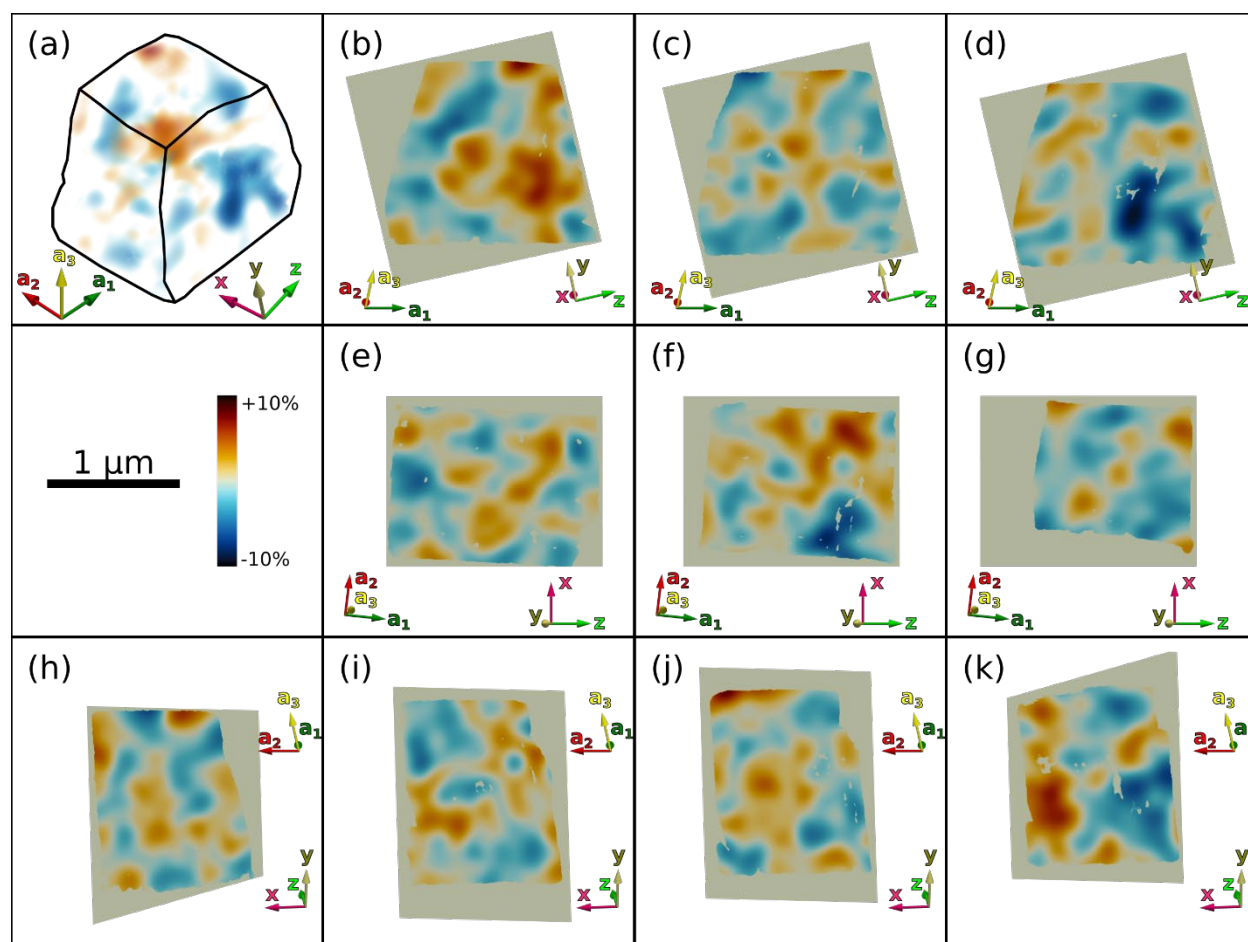


**Figure S21.** a) Volume rendering of the  $\omega_{xy}$  superlattice rotation matrix component. {010} (b-d), {001} (e-g) and {100} (h-k) 2D slices through this rotation matrix component, sliced the same way as in Figure S12.

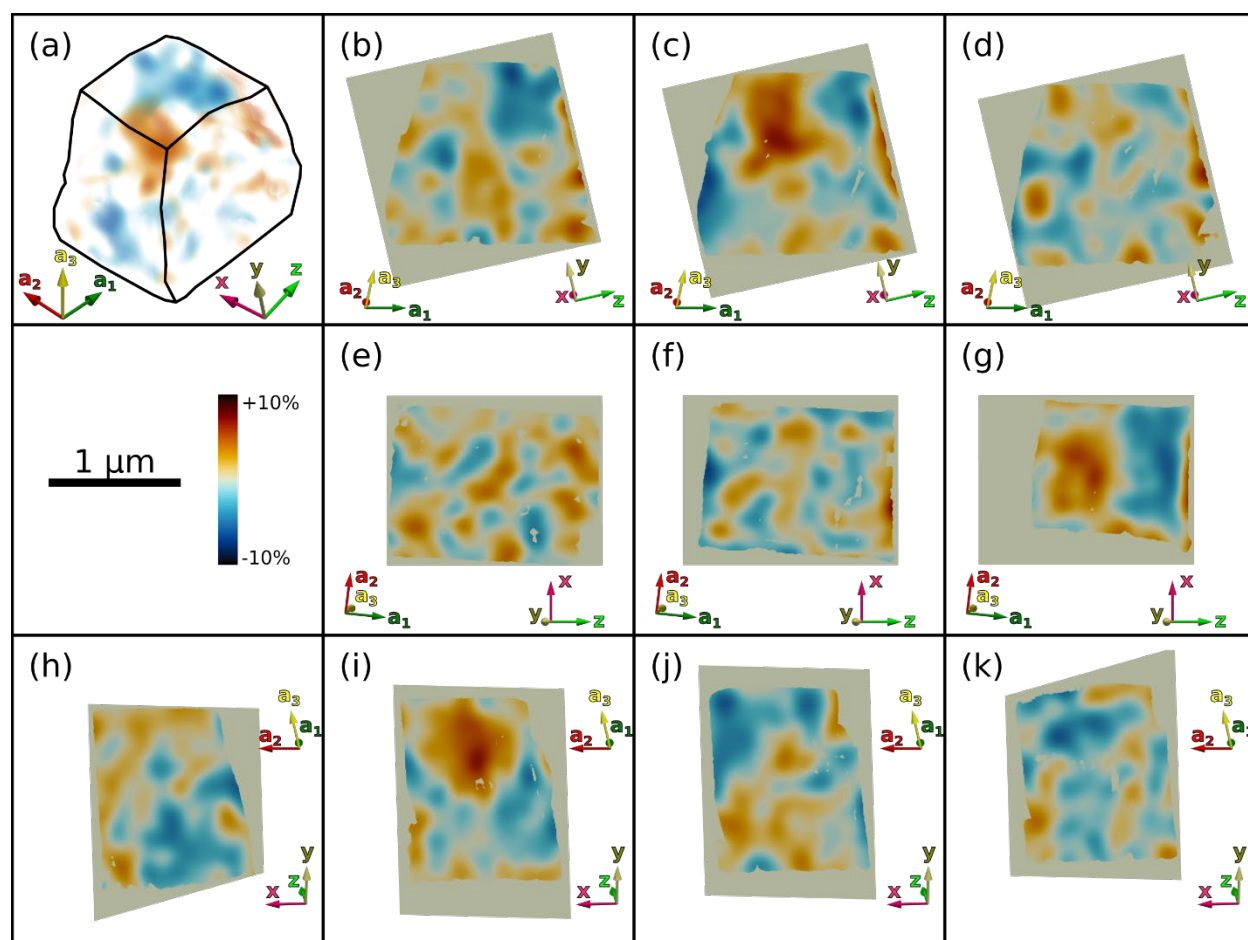


**Figure S22.** a) Volume rendering of the  $\omega_{xz}$  superlattice rotation matrix component. {010} (b-d), {001} (e-g) and {100} (h-k) 2D slices through this rotation matrix component, sliced the same way as in Figure S12.

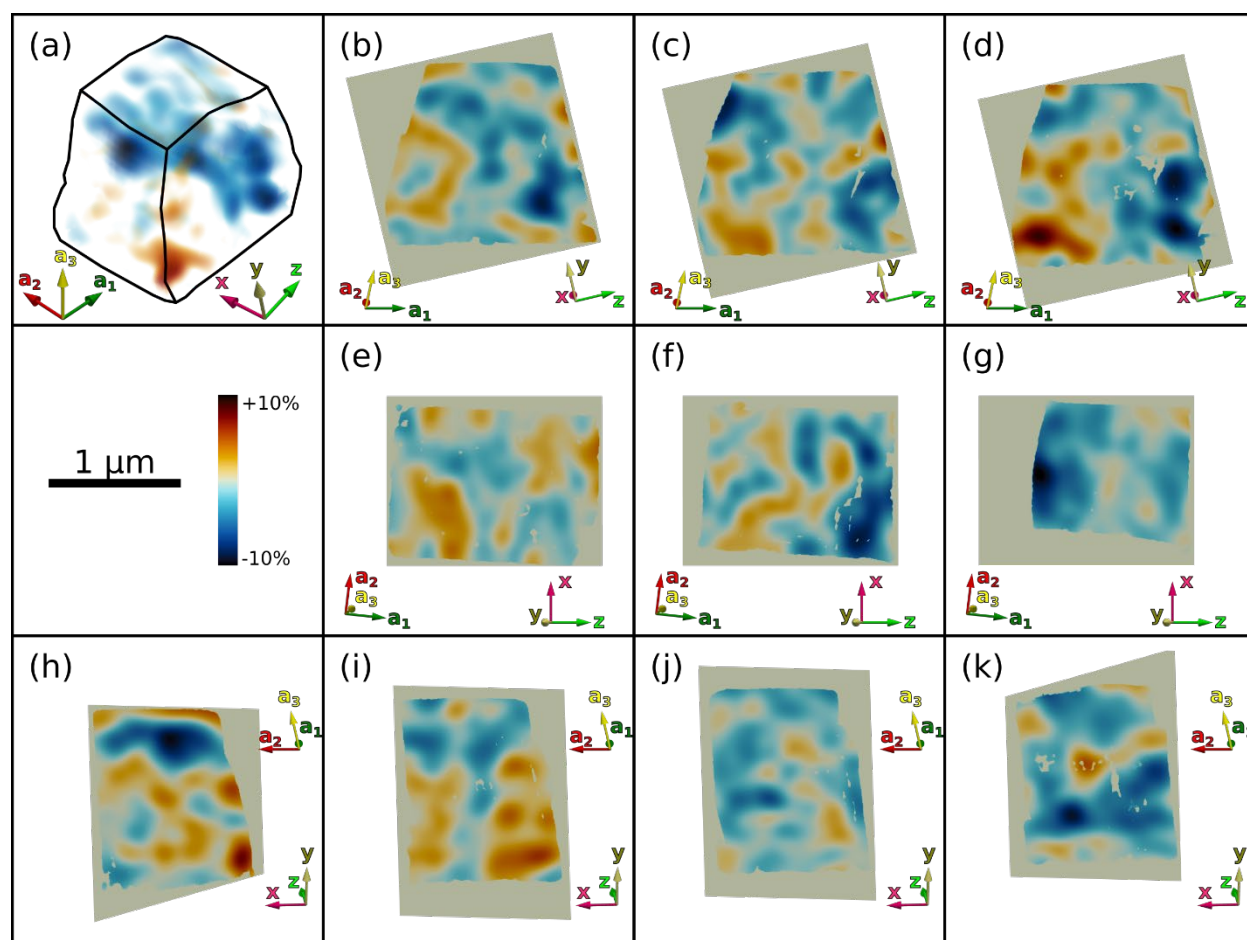


**Figure S23.** a) Volume rendering of the  $\omega_{vz}$  superlattice rotation matrix component. {010} (b-d), {001} (e-g) and {100} (h-k) 2D slices through this rotation matrix component, sliced the same way as in Figure S12.

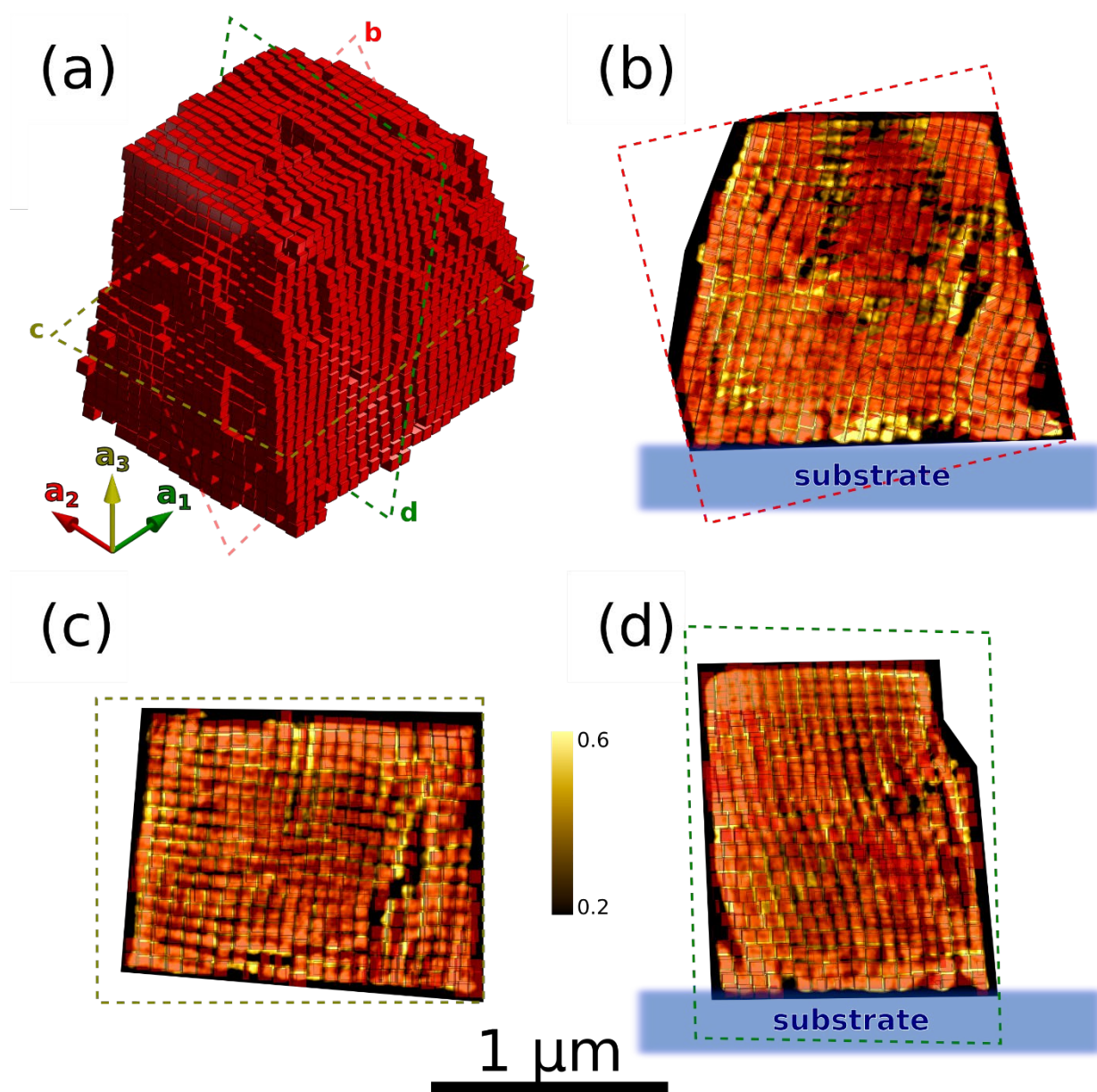


**Figure S24.** (a) Model of an ideal crystal, strained by the measured superlattice strain, verifying the fidelity of the obtained strain tensor and rotation matrix. (b-d) 2D slices parallel to (010) (b), (001) (c) and (100) (d) planes of the reconstructed mesocrystal, sliced the same way as in Figure 5, with overlay of the corresponding slice through the model in (a).

**Movie S1:** Volume rendering of the measured 3D diffraction pattern.

**Movie S2:** Volume rendering of reconstructed 3D electron density of mesocrystal.

**Movie S3a-c:** Volume rendering of reconstructed 3D electron density of mesocrystal, sliced through (100), (010) and (001) planes.

**Movie S4a-c:** Electron density of mesocrystal, sliced through (100), (010) and (001) planes.

**Movie S5:** Volume rendering of the 3D superlattice dilatation map.

**Movie S6:** Model of an ideal crystal, strained by the measured superlattice strain.

## References

1. Y. Zheng, Y. Ma, J. Zeng, X. Zhong, M. Jin, Z. Y. Li and Y. Xia, *Chem. Asian J.*, 2013, **8**, 792-799.
2. J. Zhang, J. Zhu, R. Li, J. Fang and Z. Wang, *Nano Letters*, 2017, **17**, 362-367.
3. R. Li, K. Bian, Y. Wang, H. Xu, J. A. Hollingsworth, T. Hanrath, J. Fang and Z. Wang, *Nano Letters*, 2015, **15**, 6254-6260.
4. X. Huang, J. Zhu, B. Ge, K. Deng, X. Wu, T. Xiao, T. Jiang, Z. Quan, Y. C. Cao and Z. Wang, *Journal of the American Chemical Society*, 2019, **141**, 3198-3206.
5. J. N. Clark, X. Huang, R. Harder and I. K. Robinson, *Nature Communications*, 2012, **3**, 993.
6. H. N. Chapman, A. Barty, S. Marchesini, A. Noy, S. P. Hau-Riege, C. Cui, M. R. Howells, R. Rosen, H. He, J. C. Spence, U. Weierstall, T. Beetz, C. Jacobsen and D. Shapiro, *Journal of the Optical Society of America A: Optics and Image Science, and Vision*, 2006, **23**, 1179-1200.
7. I. A. Zaluzhnyy, R. P. Kurta, M. Scheele, F. Schreiber, B. I. Ostrovskii and I. A. Vartanyants, *Materials*, 2019, **12**, 3464.
8. D. Lapkin and et al., (2021) (in preparation).
9. J. Diebel, *Matrix*, 2006, **58**.
10. P. Virtanen, R. Gommers, T. E. Oliphant, M. Haberland, T. Reddy, D. Cournapeau, E. Burovski, P. Peterson, W. Weckesser, J. Bright, S. J. van der Walt, M. Brett, J. Wilson, K. J. Millman, N. Mayorov, A. R. J. Nelson, E. Jones, R. Kern, E. Larson, C. J. Carey, Í. Polat, Y. Feng, E. W. Moore, J. VanderPlas, D. Laxalde, J. Perktold, R. Cimrman, I. Henriksen, E. A. Quintero, C. R. Harris, A. M. Archibald, A. H. Ribeiro, F. Pedregosa, P. van Mulbregt, A. Vijaykumar, A. P. Bardelli, A. Rothberg, A. Hilboll, A. Kloeckner, A. Scopatz, A. Lee, A. Rokem, C. N. Woods, C. Fulton, C. Masson, C. Häggström, C. Fitzgerald, D. A. Nicholson, D. R. Hagen, D. V. Pasechnik, E. Olivetti, E. Martin, E. Wieser, F. Silva, F. Lenders, F. Wilhelm, G. Young, G. A. Price, G.-L. Ingold, G. E. Allen, G. R. Lee, H. Audren, I. Probst, J. P. Dietrich, J. Silterra, J. T. Webber, J. Slavič, J. Nothman, J. Buchner, J. Kulick, J. L. Schönberger, J. V. de Miranda Cardoso, J. Reimer, J. Harrington, J. L. C. Rodríguez, J. Nunez-Iglesias, J. Kuczynski, K. Tritz, M. Thoma, M. Newville, M. Kümmerer, M. Bolingbroke, M. Tartre, M. Pak, N. J. Smith, N. Nowaczyk, N. Shebanov, O. Pavlyk, P. A. Brodtkorb, P. Lee, R. T. McGibbon, R. Feldbauer, S. Lewis, S. Tygier, S. Sievert, S. Vigna, S. Peterson, S. More, T. Pudlik, T. Oshima, T. J. Pingel, T. P. Robitaille, T. Spura, T. R. Jones, T. Cera, T. Leslie, T. Zito, T. Krauss, U. Upadhyay, Y. O. Halchenko, Y. Vázquez-Baeza and C. SciPy, *Nature Methods*, 2020, **17**, 261-272.
11. Z.-P. Lv, M. Kapuscinski and L. Bergström, *Nature Communications*, 2019, **10**, 4228.
12. A. Authier and A. Zarembowitch, in *International Tables for Crystallography*, 2006, DOI: <https://doi.org/10.1107/97809553602060000630>, pp. 72-98.